Liping Shi
College of Mechanical and Electrical Engineering, Nanjing University of Aeronautics and Astronautics, Nanjing 210016, China; College of Mechanical Engineering, Anhui University of Technology, Ma'anshan 243002, China

Xiuying Wang
College of Mechanical and Electrical Engineering, Nanjing University of Aeronautics and Astronautics, Nanjing 210016, China

Xiao Su
College of Mechanical and Electrical Engineering, Nanjing University of Aeronautics and Astronautics, Nanjing 210016, China

Wei Huang
College of Mechanical and Electrical Engineering, Nanjing University of Aeronautics and Astronautics, Nanjing 210016, China

Xiaolei Wang[1]
College of Mechanical and Electrical Engineering, Nanjing University of Aeronautics and Astronautics, Nanjing 210016, China
e-mail: wxl@nuaa.edu.cn

Comparison of the Load-Carrying Performance of Mechanical Gas Seals Textured With Microgrooves and Microdimples

The effects of microgrooves and microdimples on the load-carrying performance of mechanical gas seals are compared in this study. Numerical model based on the Reynolds equation for compressible Newtonian fluid is utilized to investigate the load-carrying performance including the hydrodynamic pressure, the load-carrying force, and gas film stiffness of the gas seals. The results indicate that both microgrooves and microdimples can improve the load-carrying performance of mechanical gas seals, particularly under a small clearance condition. Furthermore, different texture patterns achieve optimal load-carrying performance at different area density, seal clearance, and depth: microgrooves with a low area density can obtain higher load-carrying force and gas film stiffness than the dimple patterns, but with high area density, elliptical dimples yield better load-carrying performance than the groove patterns. [DOI: 10.1115/1.4031435]

Keywords: surface texture, mechanical gas seals, hydrodynamic effect, microgrooves, microdimples

1 Introduction

Enhancing the tribological performances of mechanical seals is of utmost importance in modern machinery for high durability and reliability. Friction force and wear increase dramatically particularly when surfaces interact under high PV[2] value conditions. Surface texturing, typically the patterns of microgrooves or microdimples fabricated on one or both of the mating interfaces, has been recognized to be an attractive approach in developing hydrodynamic pressure and improving the interfacial performance [1–9].

Since Muijderman proposed the narrow groove theory in 1965 [10], many researches have been conducted to improve tribological properties through the creation of microgrooves on the sliding surfaces of sliding bearings and mechanical seals [11–13]. Lai [14] evaluated several designs of noncontacting, nonleaking spiral grooves on the surface of liquid seal. The results demonstrated that spiral grooves could offer strong pumping capacity to eliminate fluid leakage and generate hydrodynamic lift to separate sealing faces. Qiu and Khonsari [15] studied the tribological behavior of spiral groove thrust bearing through a series of experiments. Stribeck-like curves were obtained, their characteristics were discussed, and a theoretical model was developed to gain further insight into the frictional characteristics of spiral groove in both the hydrodynamic regime and the mixed lubrication regime. Zhang et al. [16] undertook the work to make a profound investigation of the microhybrid gas spiral-grooved thrust bearing. The molecular gas film lubrication model was developed and load capacity, damping coefficients were then calculated. The results indicated that the model could serve as a useful tool to provide insight into microhybrid gas thrust bearing–rotor system. Biboulet et al. [17] developed a simplified analytical model to study the influence of cross-hatched texture on contact behavior and load-carrying capacity of oil control rings. The results indicated that this texture pattern could provide a certain load-carrying capacity which depended on the operating conditions and microgeometry of the texture, moreover, a set of functional parameters were proposed to model contact performance and predict its load-carrying capacity.

On the other hand, microdimples are another texture pattern influencing the performance of mechanical seals. In the 1960s, Hamilton et al. [18] indicated that micro-irregularities were able to generate additional hydrodynamic pressure. This theory has been well accepted and promoted, particularly by Etsion's group

[1]Corresponding author.

Contributed by the Tribology Division of ASME for publication in the JOURNAL OF TRIBOLOGY. Manuscript received January 28, 2015; final manuscript received August 13, 2015; published online October 15, 2015. Assoc. Editor: Jordan Liu.

[2]The product of contact pressure and linear velocity.

[19–25], who developed a series of theoretical models of sealing surfaces textured with microhemispherical dimples. The results suggested that improved hydrodynamic effect and film stiffness can be obtained with optimized parameters. Based on these studies, Bai et al. [26] introduced a type of laser surface texturing for gas seals, theoretical model was developed to study the influence of dimple orientation on open force and leakage. Results showed that the oriented ellipse dimples can significantly enhance hydrodynamic effect which leads to increase the open force and reduce leakage. Qiu et al. [27,28] investigated comprehensively the effects of texture shape on the friction coefficient and gas film stiffness. It was found that the ellipsoidal shape yielded the minimum friction coefficient and the highest bearing stiffness, and the result was independent of the operating conditions.

Briefly, it can be summarized that both microgrooves and microdimples could provide additional hydrodynamic effect to improve tribological characteristics of mechanical seals. Microgrooves might be the most successful pattern of surface texture by the example of cross-hatching pattern for the cylinder liner of combustion engines [13,29,30]. On the other hand, Sasaki and coworkers [31,32] indicated that independent and closed texture cells such as dimples were better to obtain hydrodynamic effect than connected structures such as grooves, which may lead to channel the lubricant away from the interface. Therefore, it is of interest to identify either microgrooves or microdimples are better for mechanical seals to obtain better load-carrying performance.

The objective of this study is to compare the load-carrying performance of mechanical gas seals textured with microgrooves and microdimples. A theoretical model based on the Reynolds equation is performed for compressible Newtonian fluid, and four kinds of texture shapes including elliptical dimples, circular dimples, closed grooves, and interpenetrating grooves are studied. Hydrodynamic pressure, the load-carrying force, and gas film stiffness under a given set of operating conditions are calculated and discussed.

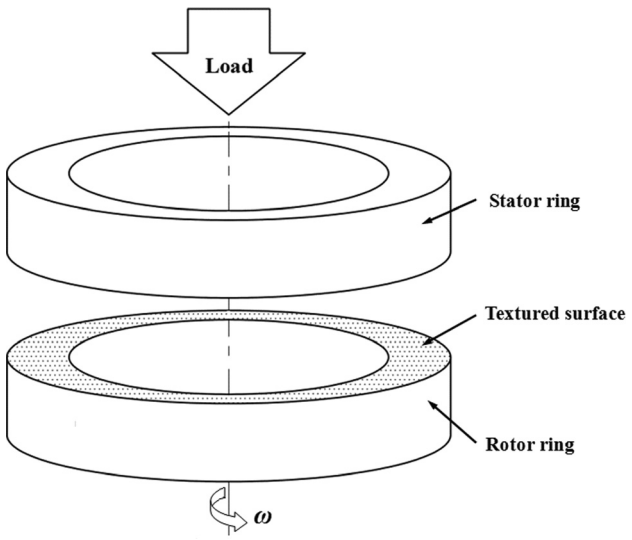

Fig. 1 Schematic diagram of a mechanical gas seal

2 Analytical Model

2.1 Equations. A schematic description of mechanical gas seals by two mating rings is presented in Fig. 1. A load is applied downward on the stator ring, the angle velocity of the rotor ring is ω. Textures are arranged on the surface of rotor ring with an area density $S_P = A/S$, where A is the area of textures and S is the area of the rotor ring surface.

Four selected texture patterns are depicted in Fig. 2. For the pattern of microdimples, the textures are distributed evenly both in the radial and circumferential directions. The long axis of elliptical dimples is parallel to the radial direction. For the pattern of microgrooves, the textures are distributed evenly in the circumferential directions, moreover, microgrooves 1 presents the case that grooves interpenetrate the inner radius of the rotor ring, and microgrooves 2 are closed and distributed in the center of the rotor ring surface. The sealing faces are separated by a uniform gas film thickness h_0 and the gas fills in the configurations with a depth of h_p. r_i and r_o represent the inner and outer radius of the rotor ring, respectively. In order to obtain accurate results, as advised in Ref. [5], studied area containing several columns is chosen in this research.

The basic assumptions in this work are given as follows: the sealed gas is compressible and viscous (Newtonian) with a constant dynamic viscosity μ; the flow in the gas film is laminar.

The two-dimensional, steady-state Reynolds equation in cylindrical coordinates is

$$\frac{\partial}{\partial r}\left(\frac{\rho r h^3}{\mu}\frac{\partial p}{\partial r}\right)+\frac{1}{r}\frac{\partial}{\partial \theta}\left(\frac{\rho h^3}{\mu}\frac{\partial p}{\partial \theta}\right)=6\omega r\frac{\partial(\rho h)}{\partial \theta} \tag{1}$$

where r and θ are the cylindrical coordinates in the radial and circumferential directions, respectively, ρ represents the gas density, p is the local hydrodynamic pressure, and h is the local film thickness.

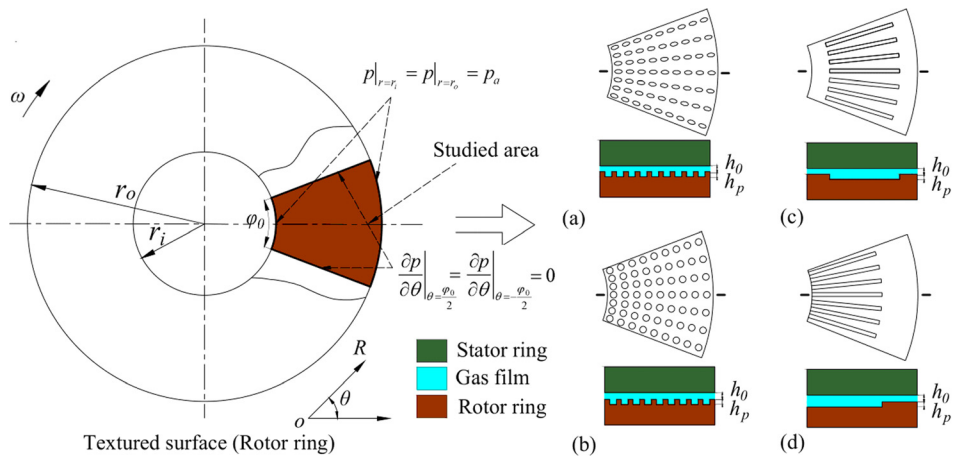

Fig. 2 The geometrical model of texture patterns: (*a*) elliptical dimples, (*b*) circular dimples, (*c*) microgrooves 1, and (*d*) microgrooves 2

At a specific point (r, θ), h can be expressed by

$$h(r,\theta) = \begin{cases} h_0 + h_p & (r,\theta) \in \Omega \\ h_0 & (r,\theta) \notin \Omega \end{cases} \tag{2}$$

where Ω is the textured region.

Assuming that the gas film between the two sealed rings is an isothermal flow, the ideal gas state equation is

$$\frac{p}{\rho} = \text{const} \tag{3}$$

Substituting Eq. (3) into Eq. (1), the Reynolds equation is derived as

$$\frac{\partial}{\partial r}\left(\frac{prh^3}{\mu}\frac{\partial p}{\partial r}\right) + \frac{1}{r}\frac{\partial}{\partial \theta}\left(\frac{ph^3}{\mu}\frac{\partial p}{\partial \theta}\right) = 6\omega r\frac{\partial (ph)}{\partial \theta} \tag{4}$$

The pressure at inner and outer radius of the rotor ring is assumed to be an atmospheric pressure. In the circumferential direction, the texture pressure changes periodically in studied area so that the boundary conditions are

$$\begin{cases} p(r = r_i, \theta) = p(r = r_o, \theta) = p_a \\ \dfrac{\partial p}{\partial \theta}\left(r, \theta = \dfrac{\varphi_0}{2}\right) = \dfrac{\partial p}{\partial \theta}\left(r, \theta = -\dfrac{\varphi_0}{2}\right) = 0 \end{cases} \tag{5}$$

where φ_0 is the central angle of studied area, and p_a is an atmospheric pressure.

Equation (4) can be written in dimensionless form as

$$\frac{1}{R}\frac{\partial}{\partial R}\left(RPH^3\frac{\partial P}{\partial R}\right) + \frac{1}{R^2}\frac{\partial}{\partial \Theta}\left(PH^3\frac{\partial P}{\partial \Theta}\right) = \Lambda\frac{\partial (PH)}{\partial \Theta} \tag{6}$$

where $R = r/r_i$, $\Theta = \theta$, $H = h/h_0$, and $P = p/p_a$, where H is the dimensionless local film thickness, P is the dimensionless local hydrodynamic pressure, and $\Lambda = (6\mu\omega/p_a)(r_i/h_0)^2$ is the seal parameter.

At a specific point (R, Θ), H is given by

$$H(R,\Theta) = \begin{cases} 1 + \dfrac{h_p}{h_0} & (R,\Theta) \in \Omega \\ 1 & (R,\Theta) \notin \Omega \end{cases} \tag{7}$$

The boundary conditions in dimensionless form are

$$\begin{cases} P(R = 1, \Theta) = P(R = r_o/r_i, \Theta) = 1 \\ \dfrac{\partial P}{\partial \Theta}\left(R, \Theta = \dfrac{\varphi_0}{2}\right) = \dfrac{\partial P}{\partial \Theta}\left(R, \Theta = -\dfrac{\varphi_0}{2}\right) = 0 \end{cases} \tag{8}$$

In order to obtain pressure distribution between the two mating surfaces, a grid of 2000×2000 nodes over the studied area is chosen based on the consideration on both computing time and accuracy, and the Reynolds Eq. (6) is solved by a finite-difference method. Then, a set of nonlinear algebraic equations are obtained. The successive over relaxation method (SOR) is used to solve these equations by combining Eq. (8), the converging condition is taken as

$$P_{i,j}^{k+1} = P_{i,j}^{k} + \chi(\bar{P}_{i,j}^{k+1} - P_{i,j}^{k}) \tag{9}$$

where χ is the SOR factor and $\chi = 1.3$ is chosen to obtain a fast convergence, $P_{i,j}^{k}$ and $P_{i,j}^{k+1}$ are the pressure values at iterative step k and $k+1$, and $\bar{P}_{i,j}^{k+1}$ are the temporary values at step $k+1$. The converging condition is confirmed as

$$\frac{\|P_{i,j}^{k+1} - P_{i,j}^{k}\|}{\|P_{i,j}^{k}\|} \le \text{Err}_P \tag{10}$$

where Err_p is the error tolerance, taken as 1.0×10^{-5} here.

2.2 Load-Carrying Performance. If the solution process is convergent, the load-carrying force and stiffness can be calculated according to the pressure distribution. By integrating the local hydrodynamic pressure, the load-carrying force, F, is obtained as follows:

$$F = \frac{2\pi}{\varphi_0}\int\int p(r,\theta) r dr d\theta = \frac{2\pi}{\varphi_0}\int_0^{\varphi_0}\int_{r_i}^{r_o} p(r,\theta) r dr d\theta \tag{11}$$

The dimensionless average pressure, P_{av}, is chosen as an index to evaluate the hydrodynamic effect and can be expressed as

$$P_{\text{av}} = \frac{F}{p_a A} \tag{12}$$

The gas film stiffness, K, is the derivative of the load-carrying force with respect to the seal clearance h_0 and can be presented as

$$K = -\frac{dF}{dh_0} \tag{13}$$

3 Results and Discussion

The main texture parameters affecting the load-carrying performance are: the type of texture patterns, area density S_P, the dimensionless seal clearance δ ($\delta = h_0/2r_p$), and the dimensionless aspect ratio ε ($\varepsilon = h_p/2r_p$).

The values of geometric parameters of the textures used in this paper are shown in Fig. 2 and Table 1.

3.1 Dimensionless Pressure Distribution. Figure 3 presents a typical dimensionless pressure distribution over the studied area under the conditions of $S_P = 23.60\%$, $\delta = 0.02$, and $\varepsilon = 0.04$. It can be found that a hydrodynamic pressure can be formed on the mating surfaces, and in the radial direction, the pressure shows a nonlinear increment with increasing radius. Obviously, the hydrodynamic effect significantly depends on the texture patterns although the area density, seal clearance, and the depth are identical in all the texture patterns. Among these patterns, the elliptical dimples obtain the best hydrodynamic effect, the dimensionless average pressure, P_{av}, can reach to 1.52, which is 13.24% higher than 1.36, that of the microgrooves 2.

3.2 The Load-Carrying Force. Figure 4 describes the effect of area density, S_P, on the load-carrying force, F, for different

Table 1 Geometric parameters values of textured mechanical gas seals

Item	Values
The inner radius of the rotor ring, r_i (mm)	15
The outer radius of the rotor ring, r_o (mm)	20
Circular dimples radius, r_p (μm)	100
The angle velocity of the rotor ring, ω (rpm)	3000
Sealed gas dynamic viscosity, μ (Pa·s)	1.79×10^{-5}
An atmospheric pressure, p_a (Pa)	1.01×10^5
Area density, S_P	7.70%, 16.80%, 23.60%, 30.40%, 39.1%, and 47.70%
The dimensionless seal clearance, δ	0.005–0.030
The dimensionless aspect ratio, ε	0.001–0.040

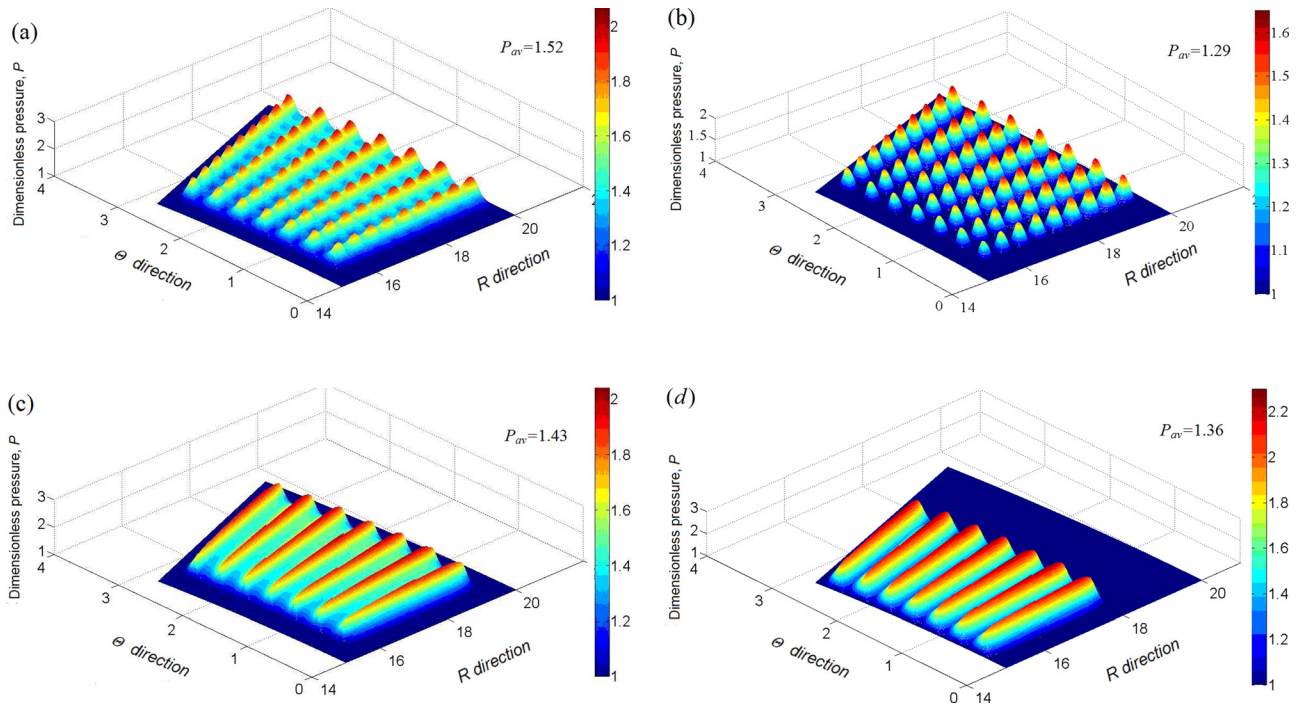

Fig. 3 Dimensionless pressure distribution at $S_P = 23.60\%$, $\delta = 0.02$, and $\varepsilon = 0.04$ for different texture patterns: (*a*) elliptical dimples, (*b*) circular dimples, (*c*) microgrooves 1, and (*d*) microgrooves 2

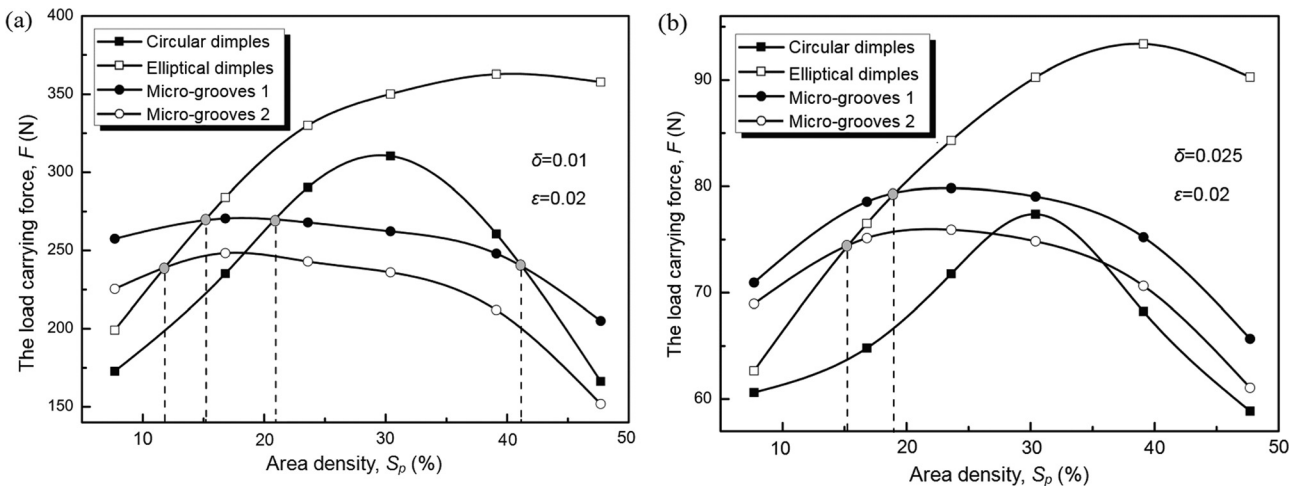

Fig. 4 Effect of area density, S_P, on the load-carrying force, F: (*a*) $\delta = 0.01$, $\varepsilon = 0.02$ and (*b*) $\delta = 0.025$, $\varepsilon = 0.02$

texture patterns. As shown in the figure, for each texture pattern, the load-carrying force first increases and then decreases with increasing area density. It means that there exists an optimal area density for the maximum load-carrying force for each pattern under the conditions of specific δ and ε (e.g., $S_P = 30.0\%$ for circular dimples at $\delta = 0.01$ and $\varepsilon = 0.02$).

Also in Fig. 4, the "pattern effect" can be observed. In Fig. 4(*a*), for the pattern of microgrooves, microgrooves 1 has larger load-carrying force than microgrooves 2, indicating that closed grooves are better to obtain hydrodynamic effect than interpenetrating structures. Comparing to the pattern of micro-dimples, the pattern of microgrooves could obtain better load-carrying force while the area density $S_P < 10\%$. However, with the increasing of area density, the load-carrying force of micro-dimples increases fast and could be higher than the pattern of microgrooves while the area density is as high as 30%. The elliptical dimples always have the load-carrying force higher than that of circular dimples. The similar effect can be observed in Fig. 4(*b*).

Figure 5 shows the effect of the dimensionless seal clearance, δ, on the load-carrying force, F, at (*a*) $\varepsilon = 0.005$, $S_P = 7.70\%$ and (*b*) $\varepsilon = 0.035$, $S_P = 39.10\%$. It can be found that the load-carrying force decreases drastically with increasing seal clearance particularly under a small clearance condition. As can be seen in Fig. 5(*a*), the value of load-carrying force is approximately from 1350 N at the minimum dimensionless seal clearance ($\delta = 0.005$) to the much lower value of 130 N at the maximum dimensionless seal clearance ($\delta = 0.030$), indicating the texture effect is more obvious at smaller seal clearance. However, when the value of δ exceeds 0.013, the load-carrying force is found to be insensitive to the increase of seal clearance. But in Fig. 5(*b*), only when the value of δ exceeds 0.030, the curves tend to be leveled.

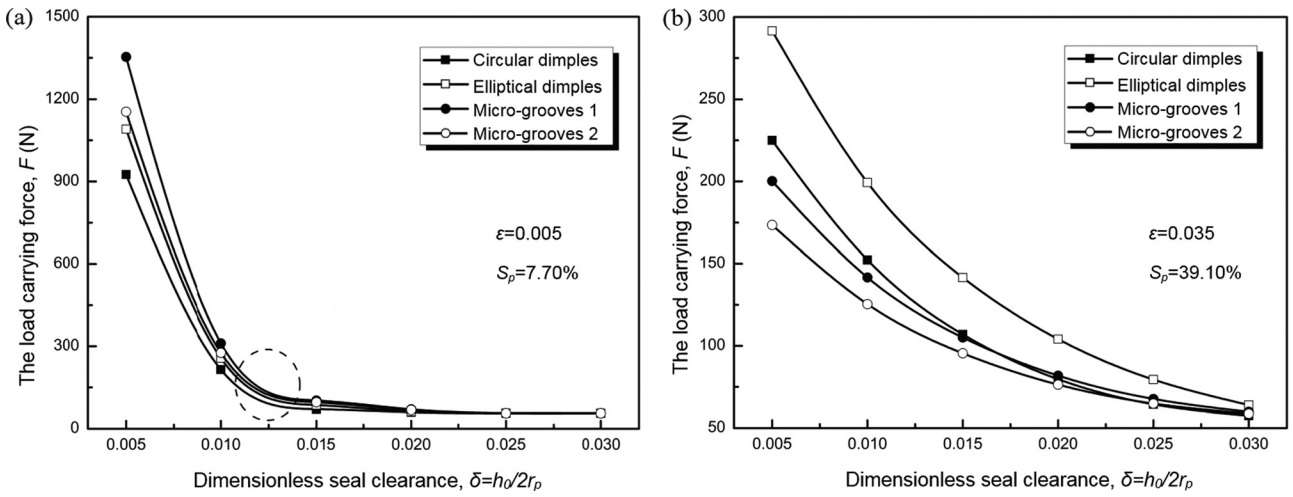

Fig. 5 Effect of dimensionless seal clearance, δ, on the load-carrying force, F: (*a*) $\varepsilon = 0.005$, $S_P = 7.70\%$ and (*b*) $\varepsilon = 0.035$, $S_P = 39.10\%$

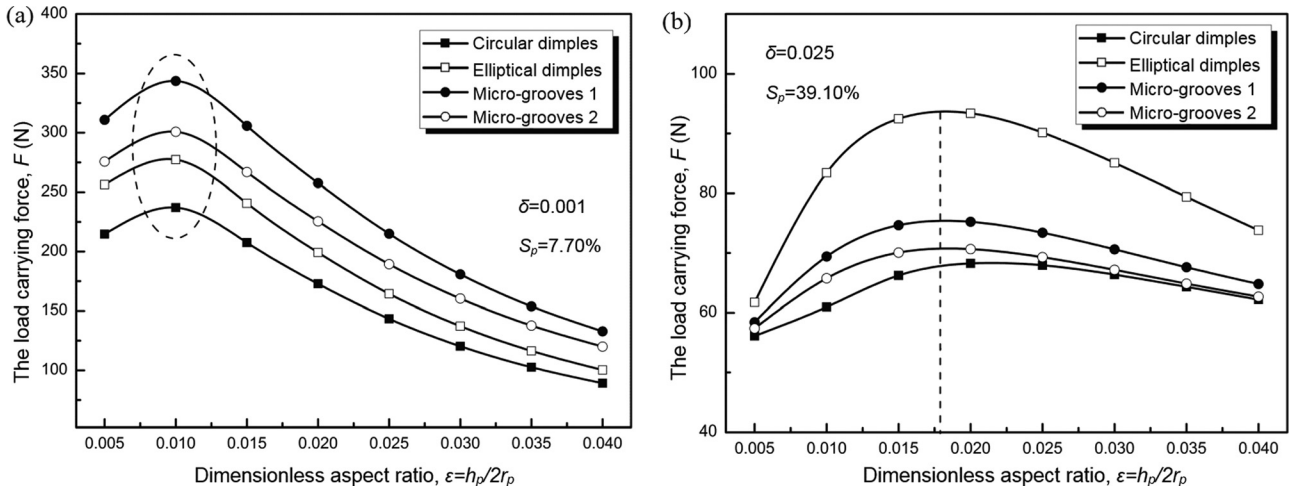

Fig. 6 Effect of dimensionless aspect ratio, ε, on the load-carrying force, F: (*a*) $\delta = 0.001$, $S_P = 7.70\%$ and (*b*) $\delta = 0.025$, $S_P = 39.10\%$

Figure 6 demonstrates the effect of the dimensionless aspect ratio, ε, on the load-carrying force, F. As shown in the figure, for each individual texture pattern, the load-carrying force first increases and then decreases with increasing aspect ratio, indicating that there exists an optimal aspect ratio to maximize the load-carrying force. It appears that the optimal values are relatively insensitive to texture patterns. On the other hand, there is a clear pattern effect on the load-carrying force, F, when $S_P = 7.70\%$, microgrooves have larger load-carrying force than microdimples (see Fig. 6(*a*)), but elliptical dimples have the largest value when $S_P = 39.10\%$ (see Fig. 6(*b*)).

3.3 Gas Film Stiffness. As shown in Fig. 5, under a small seal clearance condition, the load-carrying force is very sensitive to the change of δ. The slope of the curve represents the gas film stiffness, K.

Figure 7 depicts the effect of area density, S_P, on gas film stiffness, K, for different texture patterns at (*a*) $\delta = 0.01$, $\varepsilon = 0.02$ and (*b*) $\delta = 0.025$, $\varepsilon = 0.02$. In each figure, first, an optimal area density is clearly seen for maximum gas film stiffness for each texture pattern. Second, microgrooves 1 have larger gas film stiffness than microgrooves 2. For the pattern of dimples, elliptical dimples have larger value than circular ones. Furthermore, when area density is low ($S_P < 9.20\%$ in Fig. 7(*a*) or $S_P < 15.0\%$ in Fig. 7(*b*), microgrooves can obtain higher gas film stiffness. But when S_P is high, the elliptical dimples clearly have higher gas film stiffness than the others.

Figure 8 presents the gas film stiffness, K, as a function of the dimensionless seal clearance, δ. It can be found that the gas film stiffness increases as the dimensionless seal clearance decreases for each texture pattern. From Fig. 8(*a*), when $\delta > 0.0175$, the gas film stiffness does not change drastically and goes to a small value about $K = 1.15 \times 10^5\,\mathrm{N \cdot mm^{-1}}$. However, for $\delta < 0.0175$, it can be seen the effect of dimensionless seal clearance on the gas film stiffness is significant. The same trend can be observed in Fig. 8(*b*), but when the value of seal clearance is larger than 0.030, the gas film stiffness is almost insensitive to the seal clearance.

Figure 9 displays the effect of the dimensionless aspect ratio, ε, on gas film stiffness, K, in the cases of (*a*) $\delta = 0.001$, $S_P = 7.70\%$ and (*b*) $\delta = 0.025$, $S_P = 39.10\%$. In each figure, an optimum value of the dimensionless aspect ratio for maximum gas film stiffness is clearly seen. Moreover, by comparing the

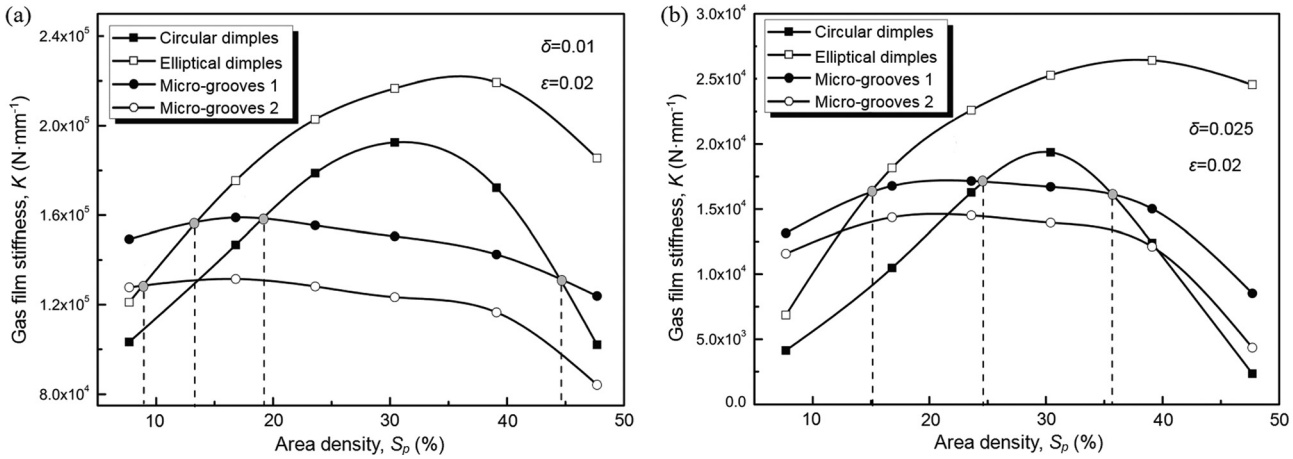

Fig. 7 Effect of area density, S_P, on gas film stiffness, K: (*a*) $\delta = 0.01$, $\varepsilon = 0.02$ and (*b*) $\delta = 0.025$, $\varepsilon = 0.02$

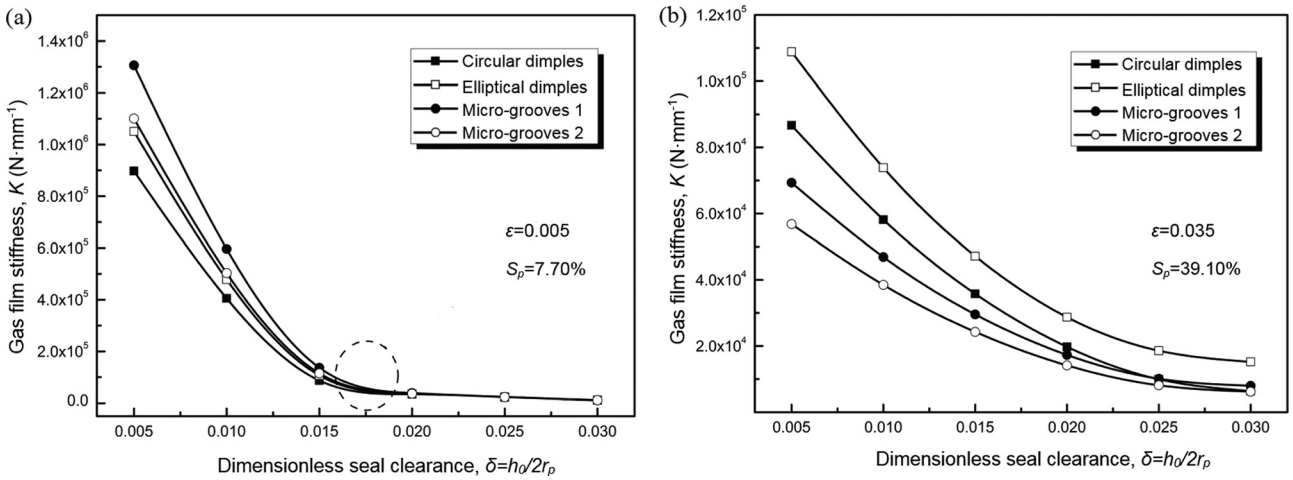

Fig. 8 Effect of dimensionless seal clearance, δ, on gas film stiffness, K: (*a*) $\varepsilon = 0.005$, $S_P = 7.70\%$ and (*b*) $\varepsilon = 0.035$, $S_P = 39.10\%$

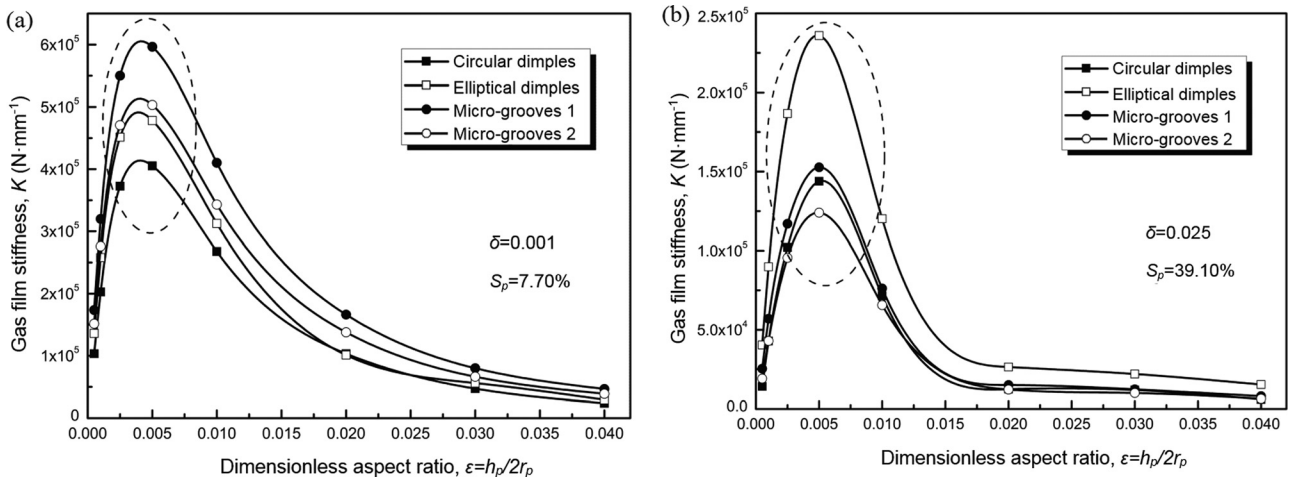

Fig. 9 Effect of dimensionless aspect ratio, ε, on gas film stiffness, K: (*a*) $\delta = 0.001$, $S_P = 7.70\%$ and (*b*) $\delta = 0.025$, $S_P = 39.10\%$

two figures, it can be found that the dimensionless aspect ratio, ε, is around 0.005 for the maximum gas film stiffness, which is independent of the type of texture patterns, area density, and the dimensionless seal clearance, similar to previous documented results [5,22].

4 Conclusions

In this study, a theoretical model was developed and the effects of microgrooves and microdimples on the load-carrying performance including the hydrodynamic pressure, the load-carrying

force, and gas film stiffness at the same area density, seal clearance, and the depth were compared. The main conclusions can be summarized as:

(1) Both microgrooves and microdimples can improve the load-carrying performance of mechanical gas seals, particularly under a small clearance condition. However, the load-carrying performance significantly depends on the texture patterns even though their area density, seal clearance, and the depth are identical.
(2) Microgrooves with a low area density can obtain higher load-carrying force and gas film stiffness, but when the area density is higher than 10%, elliptical dimples yield better load-carrying performance.
(3) For the pattern of microgrooves, closed grooves are better to obtain high load-carrying capacity than interpenetrating structures, for the pattern of microdimples, elliptical dimples with long axis paralleled to the radial direction can have better load-carrying performance than circular dimples.

Acknowledgment

The authors are grateful for the financial support provided by the National Nature Science Foundation of China (No. 51175246) and Priority Academic Program Development of Jiangsu Higher Education Institutions (PAPD).

Nomenclature

A = the area of textures
F = the load-carrying capacity
$h(r, \theta)$ = film thickness at point (r, θ)
$H(R, \Theta)$ = dimensionless film thickness at (R, Θ), $H(R, \Theta) = h(r, \theta)/h_0$
h_p = texture depth
h_0 = gas film clearance
K = gas film stiffness
$p(r, \theta)$ = hydrodynamic pressure at point (r, θ)
$P(R, \Theta)$ = dimensionless hydrodynamic pressure at (R, Θ), $P(R, \Theta) = p(r, \theta)/p_a$
p_a = an atmospheric pressure
P_{av} = dimensionless average pressure
r = coordinate in radial direction
R = dimensionless coordinate in radial direction, $R = r/r_p$
r_i = the inner radius of the rotor ring
r_o = the outer radius of the rotor ring
r_p = circular dimples radius
S = the area of the rotor ring surface
S_P = area density, $S_P = A/S$
δ = dimensionless seal clearance
ε = dimensionless aspect ratio
θ = coordinate in circumferential direction
Θ = dimensionless coordinate in circumferential direction, $\Theta = \theta$
Λ = seal parameter, $\Lambda = (6\mu\omega/p_a)(r_i/h_0)^2$
μ = sealed gas dynamic viscosity
ρ = sealed gas density
φ_0 = central angle of studied area
Ω = textured region
ω = the angle velocity of the rotor ring (rpm)

References

[1] Kligerman, Y., and Etsion, I., 2001, "Analysis of the Hydrodynamic Effects in a Surface Textured Circumferential Gas Seal," Tribol. Trans., **44**(3), pp. 472–478.
[2] Brizmer, V., Kligerman, Y., and Etsion, I., 2003, "A Laser Surface Textured Parallel Thrust Bearing," Tribol. Trans., **46**(3), pp. 397–403.
[3] Wang, X., Adachi, K., and Kato, K., 2005, "Running-in Effect on the Load-Carrying Capacity of a Water-Lubricated SiC Thrust Bearing," Proc. Inst. Mech. Eng., Part J, **219**(2), pp. 117–124.
[4] Raeymaekers, B., Etsion, I., and Talke, F. E., 2007, "A Model for Magnetic Tape/Guide Friction Reduction by Laser Surface Texturing," Tribol. Lett., **28**(1), pp. 9–17.
[5] Yu, H., Wang, X., and Zhou, F., 2009, "Geometric Shape Effects of Surface Texture on the Generation of Hydrodynamic Pressure Between Conformal Contacting Surfaces," Tribol. Lett., **37**(2), pp. 123–130.
[6] Yu, H., Deng, H., Huang, W., and Wang, X., 2011, "The Effect of Dimple Shapes on Friction of Parallel Surfaces," Proc. Inst. Mech. Eng., Part J, **225**(8), pp. 693–703.
[7] Tala-Ighil, N., Fillon, M., and Maspeyrot, P., 2011, "Effect of Textured Area on the Performances of a Hydrodynamic Journal Bearing," Tribol. Int., **44**(3), pp. 211–219.
[8] Zhang, J., and Meng, Y., 2012, "Direct Observation of Cavitation Phenomenon and Hydrodynamic Lubrication Analysis of Textured Surfaces," Tribol. Lett., **46**(2), pp. 147–158.
[9] Shen, C., and Khonsari, M. M., 2013, "Effect of Dimple's Internal Structure on Hydrodynamic Lubrication," Tribol. Lett., **52**(3), pp. 415–430.
[10] Muijderman, E. A., 1965, *Spiral Groove Bearing*, Ind. Lubr. Tribol., **17**(1), pp. 12–17.
[11] Ha, T. W., and Lee, A. S., 2000, "A Rotordynamic Analysis of Circumferentially-Grooved Pump Seals Based on a Three-Control-Volume Theory," KSME Int. J., **14**(3), pp. 261–271.
[12] Yu, T. H., and Sadeghi, F., 2001, "Groove Effects on Thrust Washer Lubrication," ASME J. Tribol., **123**(2), pp. 295–304.
[13] Yuan, S., Huang, W., and Wang, X., 2011, "Orientation Effects of Micro-Grooves on Sliding Surfaces," Tribol. Int., **44**(9), pp. 1047–1054.
[14] Lai, T., 1994, "Development of Non-Contacting, Non-Leaking Spiral Groove Liquid Face Seals," Lubr. Eng., **50**(8), pp. 625–631.
[15] Qiu, Y., and Khonsari, M. M., 2011, "Investigation of Tribological Behaviors of Annular Rings With Spiral Groove," Tribol. Int., **44**(12), pp. 1610–1619.
[16] Zhang, X., Wang, X., Liu, R., and Zhang, Y., 2013, "Modeling and Analysis of Micro Hybrid Gas Spiral-Grooved Thrust Bearing for Microengine," ASME J. Eng. Gas. Turbines Power, **135**(12), p. 122508.
[17] Biboulet, N., Bouassida, H., and Lubrecht, A. A., 2015, "Cross Hatched Texture Influence on the Load Carrying Capacity of Oil Control Rings," Tribol. Int., **82**(Part A), pp. 12–19.
[18] Hamilton, D. B., Walowit, J. A., and Allen, C. M., 1966, "A Theory of Lubrication by Micro-Irregularities," ASME J. Fluids Eng., **88**(1), pp. 177–185.
[19] Etsion, I., and Burstein, L., 1996, "A Model for Mechanical Seals With Regular Microsurface Structure," Tribol. Trans., **39**(3), pp. 677–683.
[20] Etsion, I., Kligerman, Y., and Halperin, G., 1999, "Analytical and Experimental Investigation of Laser-Textured Mechanical Seal Faces," Tribol. Trans., **42**(3), pp. 511–516.
[21] Etsion, I., and Halperin, G., 2002, "A Laser Surface Textured Hydrostatic Mechanical Seal," Tribol. Trans., **45**(3), pp. 430–434.
[22] Kligerman, Y., Etsion, I., and Shinkarenko, A., 2005, "Improving Tribological Performance of Piston Rings by Partial Surface Texturing," ASME J. Tribol., **127**(3), pp. 632–638.
[23] Feldman, Y., Kligerman, Y., and Etsion, I., 2006, "A Hydrostatic Laser Surface Textured Gas Seal," Tribol. Lett., **22**(1), pp. 21–28.
[24] Feldman, Y., Kligerman, Y., and Etsion, I., 2007, "Stiffness and Efficiency Optimization of a Hydrostatic Laser Surface Textured Gas Seal," ASME J. Tribol., **129**(2), pp. 407–410.
[25] Murthy, A. N., Etsion, I., and Talke, F. E., 2007, "Analysis of Surface Textured Air Bearing Sliders With Rarefaction Effects," Tribol. Lett., **28**(3), pp. 251–261.
[26] Bai, S., Peng, X., Li, Y., and Sheng, S., 2010, "A Hydrodynamic Laser Surface-Textured Gas Mechanical Face Seal," Tribol. Lett., **38**(2), pp. 187–194.
[27] Qiu, M., Delic, A., and Raeymaekers, B., 2012, "The Effect of Texture Shape on the Load-Carrying Capacity of Gas-Lubricated Parallel Slider Bearings," Tribol. Lett., **48**(3), pp. 315–327.
[28] Qiu, M., Minson, B. R., and Raeymaekers, B., 2013, "The Effect of Texture Shape on the Friction Coefficient and Stiffness of Gas-Lubricated Parallel Slider Bearings," Tribol. Int., **67**, pp. 278–288.
[29] Fu, Y., Ji, J., and Bi, Q., 2012, "The Influence of Partially Textured Slider With Oriented Parabolic Grooves on the Behavior of Hydrodynamic Lubrication," Tribol. Trans., **55**(2), pp. 210–217.
[30] Imai, N., and Kato, T., 2013, "Effects of Texture Patterns on Hydrodynamic and Mixed Lubrication Characteristics," Proc. Inst. Mech. Eng. Part J, **227**(8), pp. 898–904.
[31] Nakano, M., Korenaga, A., Korenaga, A., Miyake, K., Murakami, T., Ando, Y., Usami, H., and Sasaki, S., 2007, "Applying Micro-Texture to Cast Iron Surfaces to Reduce the Friction Coefficient Under Lubricated Conditions," Tribol. Lett., **28**(2), pp. 131–137.
[32] Nakano, M., Miyake, K., Korenaga, A., Sasaki, S., and Ando, Y., 2009, "Tribological Properties of Patterned NiFe-Covered Si Surfaces," Tribol. Lett., **35**(2), pp. 133–139.